# Performance tradeoff between lateral and interdigitated doping patterns for high speed carrier-depletion based silicon modulators

**Hui Yu,[1,*] Marianna Pantouvaki,[2] Joris Van Campenhout,[2] Dietmar Korn,[3] Katarzyna Komorowska,[1] Pieter Dumon,[1] Yanlu Li, [1] Peter Verheyen,[2] Philippe Absil,[2] Luca Alloatti,[3] David Hillerkuss,[3] Juerg Leuthold,[3] Roel Baets,[1] and Wim Bogaerts[1]**

[1]*Photonics Research Group, Department of Information Technology, Ghent University-imec, Center for Nano- and Biophotonics (NB Photonics), St.-Pietersnieuwstraat 41,9000 Gent, Belgium*

[2]*imec, Kapeldreef 75, 3001 Leuven, Belgium*

[3]*Institute of Photonics and Quantum Electronics (IPQ) and Institute of Microstructure Technology (IMT), Karlsruhe Institute of Technology(KIT), 76131 Karlsruhe, Germany*

[*]*hyu@intec.ugent.be*

**Abstract:** Carrier-depletion based silicon modulators with lateral and interdigitated PN junctions are compared systematically on the same fabrication platform. The interdigitated diode is shown to outperform the lateral diode in achieving a low $V_\pi L_\pi$ of 0.62 V·cm with comparable propagation loss at the expense of a higher depletion capacitance. The low $V_\pi L_\pi$ of the interdigitated PN junction is employed to demonstrate 10 Gbit/s modulation with 7.5 dB extinction ration from a 500 µm long device whose static insertion loss is 2.8 dB. In addition, up to 40 Gbit/s modulation is demonstrated for a 3 mm long device comprising a lateral diode and a co-designed traveling wave electrode.



**OCIS codes:** (250.7360) Waveguide modulators; (060.4080) Modulation; (130.3120) Integrated optics devices; (200.4650) Optical interconnects.

## References and links

1. G. T. Reed, G. Mashanovich, F. Y. Gardes, and D. J. Thomson, "Silicon optical modulators," Nat. Photonics **4**(8), 518–526 (2010).
2. L. Alloatti, D. Korn, R. Palmer, D. Hillerkuss, J. Li, A. Barklund, R. Dinu, J. Wieland, M. Fournier, J. Fedeli, H. Yu, W. Bogaerts, P. Dumon, R. Baets, C. Koos, W. Freude, and J. Leuthold, "42.7 Gbit/s electro-optic modulator in silicon technology," Opt. Express **19**(12), 11841–11851 (2011).
3. N. N. Feng, D. Feng, S. Liao, X. Wang, P. Dong, H. Liang, C. C. Kung, W. Qian, J. Fong, R. Shafiiha, Y. Luo, J. Cunningham, A. V. Krishnamoorthy, and M. Asghari, "30GHz Ge electro-absorption modulator integrated with 3 µm silicon-on-insulator waveguide," Opt. Express **19**(8), 7062–7067 (2011).
4. Y. Tang, H.-wen Chen, and J. E. Bowers, "Hybrid Electro-Refraction and Electro-Absorption Modulators on Silicon," in *Proceedings of 2011 8th IEEE Conference on Group IV photonics* (London, United Kingdom, 2011), 356–358.
5. M. R. Watts, W. A. Zortman, D. C. Trotter, R. W. Young, and A. L. Lentine, "Low-voltage, compact, depletion-mode, silicon Mach-Zehnder modulator," IEEE J. Sel. Top. Quantum Electron. **16**(1), 159–164 (2010).
6. N. N. Feng, S. Liao, D. Feng, P. Dong, D. Zheng, H. Liang, R. Shafiiha, G. Li, J. E. Cunningham, A. V. Krishnamoorthy, and M. Asghari, "High speed carrier-depletion modulators with 1.4V-cm $V_\pi L$ integrated on 0.25µm silicon-on-insulator waveguides," Opt. Express **18**(8), 7994–7999 (2010).
7. P. Dong, S. Liao, H. Liang, W. Qian, X. Wang, R. Shafiiha, D. Feng, G. Li, X. Zheng, A. V. Krishnamoorthy, and M. Asghari, "High-speed and compact silicon modulator based on a racetrack resonator with a 1 V drive voltage," Opt. Lett. **35**(19), 3246–3248 (2010).
8. M. Ziebell, D. Marris-Morini, G. Rasigade, P. Crozat, J. M. Fédéli, P. Grosse, E. Cassan, and L. Vivien, "Ten Gbit/s ring resonator silicon modulator based on interdigitated PN junctions," Opt. Express **19**(15), 14690–14695 (2011).
9. X. Xiao, Z. Li, Y. Hu, Y. Yu, and J. Yu, "Misalignment-tolerant High-speed Silicon Microring Modulator with Interleaved p-n Junctions," in *Proceedings of 2011 8th IEEE Conference on Group IV photonics* (London, United Kingdom, 2011), 359–361.

#166477 - $15.00 USD Received 12 Apr 2012; revised 12 May 2012; accepted 13 May 2012; published 23 May 2012

10. D. J. Thomson, F. Y. Gardes, Y. Hu, G. Mashanovich, M. Fournier, P. Grosse, J.-M. Fedeli, and G. T. Reed, "High contrast 40Gbit/s optical modulation in silicon," Opt. Express **19**(12), 11507–11516 (2011).
11. F. Y. Gardes, D. J. Thomson, N. G. Emerson, and G. T. Reed, "40 Gb/s silicon photonics modulator for TE and TM polarisations," Opt. Express **19**(12), 11804–11814 (2011).
12. L. Liao, A. Liu, D. Rubin, J. Basak, Y. Chetrit, H. Nguyen, R. Cohen, N. Izhaky, and M. Paniccia, "40 Gbit/s silicon optical modulator for high speed applications," Electron. Lett. **43**(22), 1196–1197 (2007).
13. T.-Y. Liow, K. Ang, Q. Fang, J. Song, Y. Xiong, M. Yu, G. Lo, and D. Kwong, "Silicon modulators and germanium photodetectors on SOI: Monolithic integration, compatibility, and performance optimization," IEEE J. Sel. Top. Quantum Electron. **16**(1), 307–315 (2010).
14. D. Taillaert, P. Bienstman, and R. Baets, "Compact efficient broadband grating coupler for silicon-on-insulator waveguides," Opt. Lett. **29**(23), 2749–2751 (2004).
15. H. Yu, W. Bogaerts, and A. De Keersgieter, "Optimization of ion implantation condition for depletion-type silicon optical modulators," IEEE J. Quantum Electron. **46**(12), 1763–1768 (2010).
16. W. Bogaerts, S. K. Selvaraja, P. Dumon, J. Brouckaert, K. De Vos, D. Van Thourhout, and R. Baets, "Silicon-on-Insulator Spectral Filters Fabricated With CMOS Technology," IEEE J. Sel. Top. Quantum Electron. **16**(1), 33–44 (2010).
17. Z. Y. Li, D. X. Xu, W. R. McKinnon, S. Janz, J. H. Schmid, P. Cheben, and J. Z. Yu, "Silicon waveguide modulator based on carrier depletion in periodically interleaved PN junctions," Opt. Express **17**(18), 15947–15958 (2009).
18. D. Samara-Rubio, U. D. Keil, Ling Liao, T. Franck, Ansheng Liu, D. W. Hodge, D. Rubin, and R. Cohen, "Customized drive electronics to extend silicon optical modulators to 4 Gb/s," J. Lightwave Technol. **23**(12), 4305–4314 (2005).
19. H. Yu and W. Bogaerts, "An equivalent circuit model of the traveling wave electrode for carrier-depletion-based silicon optical modulators," J. Lightwave Technol. **30**(11), 1602–1609 (2012).
20. J. Shin, S. R. Sakamoto, and N. Dagli, "Conductor loss of capacitively loaded slow wave electrodes for high-speed photonic devices," J. Lightwave Technol. **29**(1), 48–52 (2011).

## 1. Introduction

A compact, power efficient and high-speed integrated silicon modulator is a key building block of silicon photonics, a promising technology to overcome the bottleneck of current electrical interconnect systems [1]. Electric-optical modulation in silicon can be implemented by exploiting the free carrier dispersion effect of silicon itself, or by incorporating various electrical-optical materials such as polymer [2], Ge [3], and III-V compound semiconductor [4], into silicon-on-insulator (SOI) platform. Among all candidates, the carrier-depletion based modulator is the most prevailing solution due to its merits of CMOS compatibility, fabrication simplicity, and high operation speed. In these structures, a PN junction is embedded inside a silicon waveguide, and is used to manipulate the refractive index of the same waveguide by applying a reverse bias. An optical interferometer then converts the refractive index modulation to an optical intensity modulation.

The performance metrics of a PN junction based phase shifter include the modulation efficiency $V_{\pi}L_{\pi,}$, the propagation loss, and the capacitance and the series resistance of the diode. They directly determine the performance of a Mach-Zehnder modulator (MZ), in terms of required device length and drive voltage for achieving a specified dynamic extinction ratio (ER), insertion loss (IL), bit rate, and 3 dB bandwidth. In addition, the high-speed performance of a MZ modulator also depends on the type of implemented electrode, for which both lumped and traveling wave electrodes can be considered. The modulation efficiency of a PN junction based phase shifter is determined by the overlap between the space charge region and the optical mode, while the modulation speed is limited by the depletion capacitance of the PN junction. In addition, the propagation loss is determined by the overlap between free carriers and the optical mode. Therefore, the geometry of PN junction, i.e. the doping pattern, is a critical design parameter for optimizing the modulator performance. Many doping patterns have been demonstrated with specific highlights such as high modulation efficiency [5–8], better tolerance to misalignment [9,10], polarization independence [11], high operation speed [10–12], and monolithic integration with Germanium photodetectors [13]. However, these demonstrations were implemented by utilizing different waveguide dimensions, electrode designs, and ion implantation conditions.

#166477 - $15.00 USD Received 12 Apr 2012; revised 12 May 2012; accepted 13 May 2012; published 23 May 2012

A fair comparison of different doping patterns on the same fabrication and characterization platform is missing so far.

In this paper, the two most widely used doping patterns, i.e. the lateral and the interdigitated PN junctions, are systematically compared on the same platform. The result of such a comparison can serve as a reference for choosing the proper doping pattern according to the particular application. To make a complete comparison, the paper is organized as follows. First, a description of the device fabrication is given in section 2. Next, the geometries of both lateral and interdigitated PN junctions are optimized in terms of high modulation efficiency in section 3. Static modulation efficiencies $V_\pi L_\pi$ of 0.62 V·cm and 1.19 V·cm are demonstrated for interdigitated and lateral PN junctions respectively. After that, the optimized PN junctions are incorporated into MZs with the lumped electrode in section 4. The aforementioned specs of the MZ modulator are then characterized and compared. Subsequently, in section 5, up to 40 Gbit/s modulation is demonstrated for a MZ modulator with the lateral PN junction and an optimized traveling-wave electrode. Error-free modulation is demonstrated up to 35 Gbit/s. Finally we come to a conclusion in section 6.

## 2. Diode design and device fabrication

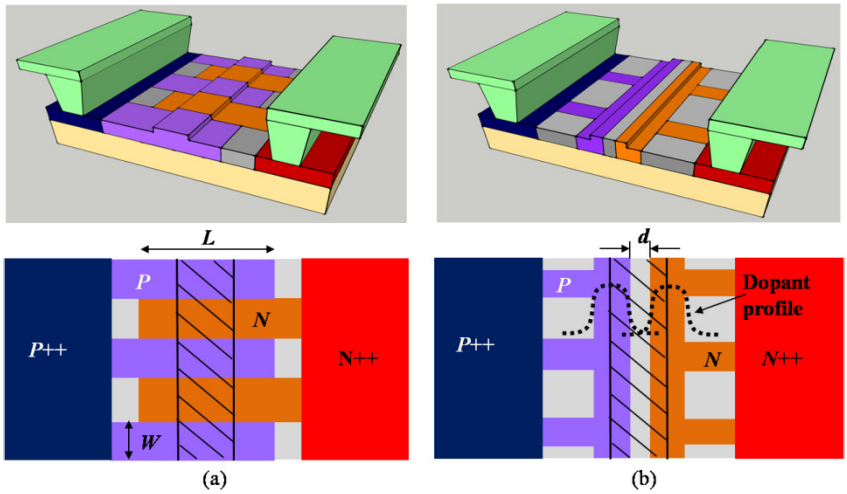


Fig. 1. Schematic 3D diagrams and top views of the two doping patterns: (a) interdigitated PN junction; (b) lateral PN junction. Shaded areas in top views mark positions of rib waveguides.

Schematic diagrams of the two competing doping patterns, i.e. the interdigitated and the lateral junctions, are presented in Fig. 1. The interdigitated diode consists of P-type and N-type fingers which alternate along the beam propagation direction, while the lateral diode has its two sides doped with opposite polarities. The width and height of the rib waveguide accommodating the PN junctions are 500 nm and 220 nm respectively. The slab height of 150 nm was chosen in order to enable simple co-integration of the diode modulators with shallowly etched fiber grating couplers [14]. The P-type and the N-type regions which form the PN junction have the same doping concentration. In addition to the diode configuration, two doping levels are compared: $1 \times 10^{18}/cm^3$ and $2 \times 10^{18}/cm^3$. The Ohmic contact regions which reside 1 µm away from the sidewall of the rib are heavily doped to $1 \times 10^{20}/cm^3$.

The modulators were fabricated on a 200-mm SOI wafer with 2 µm buried oxide and 220 nm top c-Si layer. First, the shallow-etched structures like fiber grating couplers and phase shifters were defined by 193 nm lithography and 70 nm silicon dry etching. A second 193 nm lithography step followed by 220 nm silicon dry etching then defined the strip access waveguides. Next, a 10-nm oxide layer was thermally grown to prevent ion channeling during ion implantation. The boron and phosphorous implants were carried out using photoresist as

#166477 - $15.00 USD Received 12 Apr 2012; revised 12 May 2012; accepted 13 May 2012; published 23 May 2012

the mask. Local implantation windows were opened in this resist mask using 248 nm lithography. The implantation energies were chosen to align the peak of dopant profile at the center of the silicon layer. Typical values are 25 keV for boron and 75 keV for phosphorous according to our simulation [15]. Both tilt and twist angles during implantation are kept at 0 degrees. In [15] we show that a tilt implantation angle helps to reduce the optical loss by decreasing the effective area which can be implanted at the bottom of implantation windows. However, this technique is not applicable to the ring structures on the same wafer and therefore is not utilized. The implantation dose is determined by the product of the target average doping concentration and the silicon layer thickness. For example, the dose is $2.2 \times 10^{13}/cm^2$ to achieve an average concentration of $1 \times 10^{18}/cm^3$. The dopants were subsequently activated by rapid thermal annealing (RTA) of 1075 °C. The simulated dopant distributions inside the waveguide after annealing are shown in Fig. 2, as well as the mode intensity profile of the TE-polarized guided optical mode.

Subsequently, silicide ohmic contacts were selectively formed on the highly doped contact regions, after deposition and patterning of a thin oxide layer to prevent silicidation of the silicon waveguides. This was followed by pre-metal dielectric deposition, contact holes patterning, tungsten filling and chemical mechanical polishing (CMP). Finally, the electrode was formed by a Cu-damascene process.

An asymmetrical MZ modulator is utilized to evaluate the performance of both diodes. Two compact, low-loss 1 × 2 multi-mode interferometers (MMI) are used to split and combine the optical beam [16]. Both arms of the MZ modulator contain a PN junction to balance the optical loss.

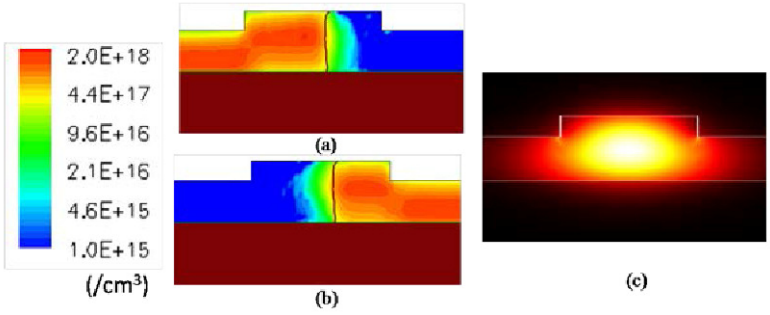


Fig. 2. Profiles of phosphorus distribution (a), boron distribution (b), and optical mode (c) inside the waveguide. TCAD tool is used to calculate the ion distribution after implantation and annealing.

## 3. Optimization of static modulation efficiency

### *3.1 Interdigitated diode*

Once the waveguide dimension and the doping concentration are fixed, the modulation efficiency of the interdigitated PN junction depends on the width $W$ of interdigitated implantation windows and the overlap length $L$ between two adjacent windows. By shrinking the window width $W$, we increase the density of PN junctions along the beam propagation direction. As such, we can expand the volume of the carrier depletion region inside the waveguide, and we can expect to obtain high modulation efficiency combined with low optical loss. Interdigitated PN junctions of $W$ = 250 nm, 300 nm and 400 nm are implemented in this study. Figure 3 shows the simulation result of the modulation efficiency and the depletion capacitance of the interdigitated PN junction with $W$ = 300 nm and $1 \times 10^{18}/cm^3$ doping concentration, as a function of the overlap length $L$. It can be seen that the modulation efficiency can be improved up to 1.12 V·cm by extending the overlap length $L$ beyond 1.6 μm. In this case, the whole optical mode inside the silicon waveguide is covered by the PN

#166477 - $15.00 USD Received 12 Apr 2012; revised 12 May 2012; accepted 13 May 2012; published 23 May 2012

junction in the lateral direction, as can be understood from the lateral spatial extent of the optical mode profile depicted in Fig. 2(c). Accordingly, the length $L$ is fixed at 1.6 µm throughout this paper for obtaining maximum modulation efficiency. However, as can be seen in Fig. 3, extending the overlap length $L$ scales up the junction area as well as the depletion capacitance, so a trade off can be expected between the modulation efficiency and speed. This will be discussed in detail in section 3.3.

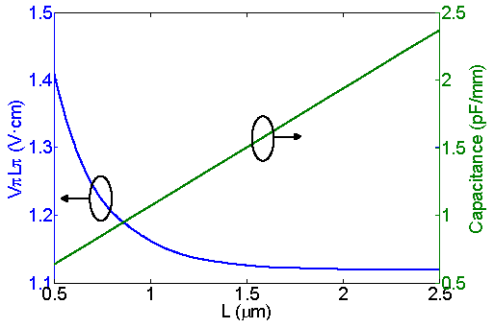


Fig. 3. Simulated modulation efficiency and capacitance of the interdigitated PN junction as a function of the overlap length $L$ between two adjacent interdigitated arms. The doping concentration and the width $W$ during the simulation is $1 \times 10^{18}/cm^3$ and $W$ = 300 nm respectively.

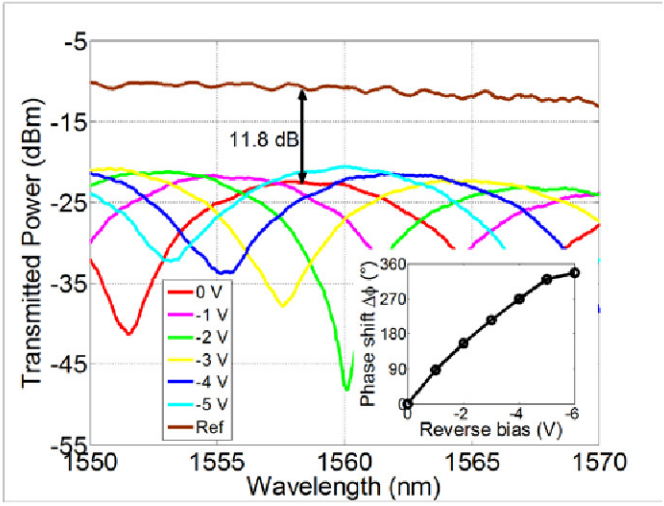


Fig. 4. Measured transmission spectra of a 3 mm long MZ modulator with an interdigitated PN junction with $W$ = 250 nm. The length difference between the two arms is 40 µm. The doping concentration is $2 \times 10^{18}/cm^3$. The inset shows the phase shift as a function of reverse bias.

Figure 4 shows the measured transmission spectra of a MZ modulator whose phase shifter length and interdigitated implantation window width are 3 mm and 250 nm respectively. The output of a passive waveguide with the same length is shown together as a reference. The total insertion loss is 11.8 dB which includes a loss of 1.5 dB from two MMIs and 4 rib-to-strip waveguide transitions. The relative phase shift $\Delta\varphi$ induced by the reverse bias $V_{bias}$ can be extracted from the transmission spectra using the equation $\Delta\varphi = 2\pi\Delta\lambda/FSR$. In this equation, FSR is the free spectral range of the asymmetric MZI and $\Delta\lambda$ is the wavelength shift due to $V_{bias}$. The results are shown in the inset of Fig. 4.

The modulation efficiency $V_\pi L_\pi$ is then deduced from $\Delta\varphi$ using $V_\pi L_\pi = \pi V_{bias} L_{ph}/\Delta\varphi$, where $L_{ph}$ is the length of phase shifter, according to its typical definition [6,13]. The

#166477 - $15.00 USD Received 12 Apr 2012; revised 12 May 2012; accepted 13 May 2012; published 23 May 2012

modulation efficiency $V_\pi L_\pi$ and the propagation loss of the phase shifter with $W$ = 250 nm and $2 \times 10^{18}$ /cm$^3$ doping concentration are plotted as a function of the reverse bias in Fig. 5. The DC modulation efficiency $V_\pi L_\pi$ corresponding to a reverse bias from 0 V to −1 V is 0.62 V·cm. This value degrades to 0.96 V·cm as the reverse bias voltage increases to −6 V. In Fig. 5, we also show the performance of the interdigitated PN junctions with $W$ = 300 nm and $W$ = 400 nm. As expected, the narrowest implantation window gives the highest modulation efficiency as well as the lowest insertion loss. For a given doping concentration and bias voltage, the maximum modulation efficiency can be expected when $W$ is close to the width of carrier depletion region [17]. Since the doping concentration is $2 \times 10^{18}$/cm$^3$ here, a reverse bias of −6 V in Fig. 5 leads to a carrier depletion region of 94 nm if an ideal abrupt PN junction is assumed. However, the practical width and pitch of the implantation windows cannot be substantially smaller than 250 nm and 500 nm respectively, due to the limited resolution of 248 nm lithography. We speculate that the DC modulation efficiency of this doping pattern can be further improved if we would enhance the lithography resolution by switching to 193 nm lithography.

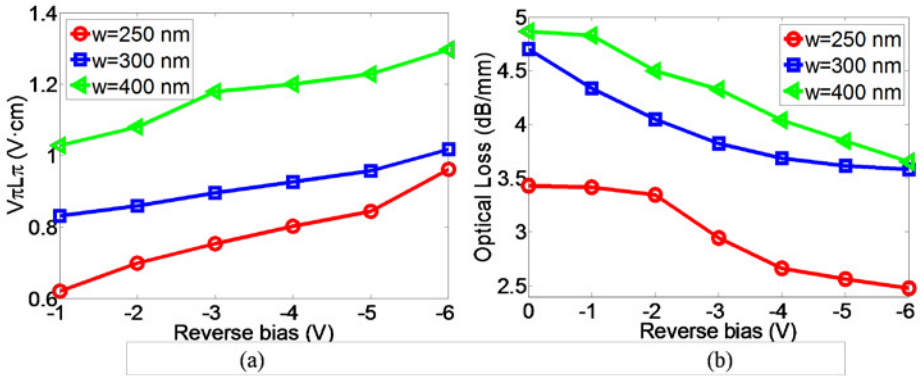


Fig. 5. Measured modulation efficiency $V_\pi L_\pi$ (a) and the optical loss (b) as a function of the reverse bias for interdigitated PN junction embedded waveguides. The doping concentration is $2 \times 10^{18}$/cm$^3$.

### *3.2 Lateral diode*

A critical parameter which has to be optimized for the lateral PN junction is the gap $d$ between the P and the N implantation windows as shown in Fig. 1(b). According to PN junction theory, an abrupt PN junction will give the highest modulation efficiency. However, a gradient PN junction is inevitable due to the lateral ion straggling during implantation and the subsequent ion diffusion during RTA. Practical dopant profiles are schematically shown in Fig. 2. A steep PN junction then is desirable for high efficiency modulation. The lateral straggling can statistically be described by a Gaussian distribution, so we can adjust the gradient of the net doping concentration in the junction area by varying the gap $d$ between the two implantation windows. Our previous simulation shows that a gap of $d$ = 40 nm gives the highest modulation efficiency [15]. This agrees well with the measurement result in Fig. 6, where we sweep $d$ from −80 nm to 160 nm. For the optimal structure of $d$ = 40 nm, the modulation efficiencies $V_\pi L_\pi$ corresponding to reverse biases of −1 V and −6 V are 1.19 V·cm and 1.23 V·cm respectively. Figure 6 also shows that the expense of enhancing the modulation efficiency is an increase of the optical loss.

#166477 - $15.00 USD Received 12 Apr 2012; revised 12 May 2012; accepted 13 May 2012; published 23 May 2012

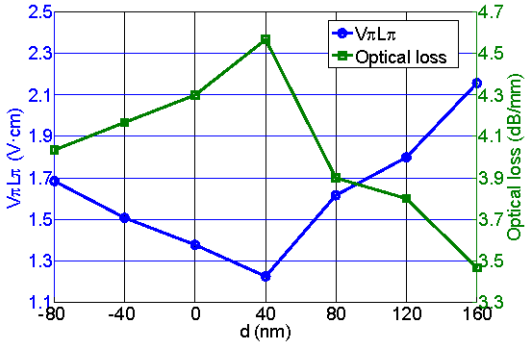


Fig. 6. Measured modulation efficiency $V_\pi L_\pi$ and optical loss of the lateral PN junction as a function of the gap $d$ between the P and the N implantation windows. $V_\pi L_\pi$ corresponds to a reverse bias of –6 V. The doping concentration is $2 \times 10^{18}/cm^3$.

### *3.3 Comparison of the lateral and interdigitated diodes*

In this section, we compare the two doping patterns. According to the optimization result in section 3.1 and 3.2, the gap between the P and the N implantation windows of the lateral PN junction is $d$ = 40 nm, while for the interdigitated PN junction the width and length of the implantation window are fixed at $W$ = 300 nm and $L$ = 1.6 μm. The DC performance of both doping patterns is shown in Fig. 7 for a doping concentration of $1 \times 10^{18}/cm^3$. Comparing Fig. 7 with Fig. 5 and 6, we find as doping concentration increases from $1 \times 10^{18}/cm^3$ to $2 \times 10^{18}/cm^3$, the loss doubles, and the modulation efficiency is enhanced by 56% and 68% for interdigitated and lateral PN junctions respectively, which agrees with the expectation. A point needs to be clarified is that with the doping concentration of $1 \times 10^{18}/cm^3$, the modulation efficiency and the optical loss exhibit the same dependences on the parameters $W$ and $d$ as presented in Figs. 5 and 6. For example, as the doping concentration is $1 \times 10^{18}$/cm3, we measured that $V_\pi L_\pi$ of interdigitated PN junctions with $W$ = 250 nm, 300 nm and 400 nm at –6 V are 1.38 V·cm, 1.5 V·cm, and 2.06 V·cm, respectively. The simulated performance of an ideal abrupt lateral PN junction with a uniform doping concentration of $1 \times 10^{18}/cm^3$ is depicted in Fig. 7 as well, which is the theoretical limit of this doping pattern at the given doping level. TCAD tool is utilized to simulate the free carrier distribution inside the abrupt PN junction with different biases. After that the carrier distribution is converted to the distribution of the refractive index through the free-carrier dispersion relationship at 1.55 $\mu$m [1]. Finally, an optical model solver is used to calculate the variation of the effective index and the optical loss as a function of the bias [15].

Next, C-V measurements were performed at 100 kHz to evaluate the depletion capacitance per unit length of both diode types. The measured capacitances at 0V were 0.44 pF/mm and 1.59 pF/mm for the lateral and the interdigitated PN junctions respectively, as shown in Fig. 7(c). Based on the well-known PN junction theory, we can calculate the depletion capacitance of ideal abrupt lateral and interdigitated PN junctions with a uniform doping concentration of $1 \times 10^{18}/cm^3$ on both P and N sides. The calculated C-V curves are shown in Fig. 7(c) as well, and they show good agreement with the measured C-V curves.

Compared with the lateral PN junction, the capacitance of interdigitated PN junction is a factor 3.6 higher. This ratio can be understood by estimating the PN junction area of each doping pattern. First, the area of lateral PN junction per unit length is 0.22 $\mu m^2/\mu m$. From the overlap length $L$ of the interdigitated PN junction and the geometry of the rib waveguide, it is easy to deduce the area of PN junction formed by two adjacent implant windows to be 0.275 $\mu m^2$. As such, the total junction area of the interdigitated PN diode is 0.907 $\mu m^2/\mu m$ for $W$ equal to 300 nm. Therefore, the junction area ratio of the two doping patterns is 4.1. This value is close to the measured ratio between the capacitances of the two doping patterns at

#166477 - $15.00 USD Received 12 Apr 2012; revised 12 May 2012; accepted 13 May 2012; published 23 May 2012

0V, which is 3.6. However, the modulation efficiency of the interdigitated PN junction is only 40% higher than that of the lateral diode. An explanation is that the carrier depletion region of lateral PN junction overlaps better with the center of optical mode where any variation of carrier density can alter the mode refractive index more effectively.

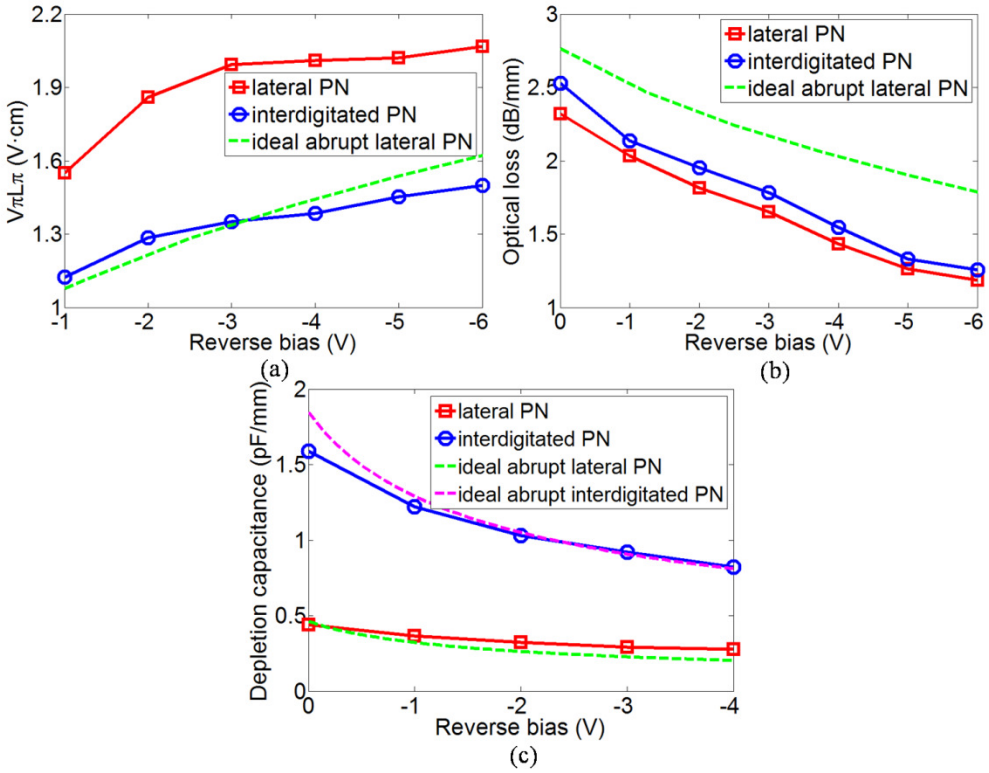


Fig. 7. Measured and simulated $V_\pi L_\pi$ (a), optical loss (b) and depletion capacitance (c) as a function of the reverse bias for the interdigitated and the lateral PN junctions. The doping concentration is $1 \times 10^{18}/cm^3$.

One point needs to be clarified about the interdigitated PN junction is that *L* is as long as 1.6 μm so as to maximize the modulation efficiency but without considering the tradeoff between the modulation efficiency and the modulation speed. By reducing *L*, we expect that the capacitance of interdigitated PN junction can be substantially reduced without a substantial reduction of the modulation efficiency. This is clear in Fig. 3. For example, if the value of *L* is 0.8 μm instead of 1.6 μm, the capacitance can be reduced from 1.59 pF/mm to 0.9 pF/mm, with a small degradation of the modulation efficiency from 1.12 V·cm to 1.2 V·cm.

Finally, the static series resistance of both diodes was extracted from the slope of the measured I-V curves under forward bias, well above the diode turn-on at around 1V. For the lateral PN junction based phase shifters, a resistance of 6.6 Ω and 5.7 Ω was measured for a 0.5mm and 1.5mm long device respectively. For the interdigitated PN junction based phase shifters of the same lengths, the extracted series resistances were 6.4 Ω and 6.3 Ω respectively.

## 4. RF electro-optical characterization of MZs with lumped electrode

In this section, we compare the RF performance of Mach-Zehnder modulators with the two doping patterns, when they are driven through lumped electrodes. The frequency responses of

#166477 - $15.00 USD Received 12 Apr 2012; revised 12 May 2012; accepted 13 May 2012; published 23 May 2012

both modulator types are studied firstly by measuring their S11 parameter (RF reflection) from 100 MHz to 40 GHz at 0 V reverse bias. The results are shown for 0.5mm and 1.5mm long devices in Fig. 8. As lumped electrodes are utilized, these modulators can be represented by the RLC circuit shown in the inset of Fig. 8(a) [18]. $C_0$ is the capacitance of contact pad, $C_1$ and $R_1$ denote the capacitance and the series resistance of diode, $L_1$ is the inductance of electrode. Values of these elements are extracted from the S11 data by curve fitting and are listed in Table 1. The dashed lines in Fig. 8 depict the curve fitting result. We find that for the 0.5 mm long diodes, the RLC circuit model can provide a good fit to the measured S11 curves of both doping patterns in the whole frequency range. However, for the 1.5 mm long diodes, the RLC model fails to provide a good fit beyond 12 GHz. That is due to the fact that at these frequencies, the diode length exceeds one tenth of the microwave wavelength; therefore the phase shifter can no longer be regarded as a lumped element and the transmission-line effect should be taken into account. Because of the skin effect, $R_1$ in the AC regime is larger than its DC value as shown in Table 1. On the other hand the diode capacitance $C_1$ extracted from S11 agrees well with the C-V measurement at 100 kHz.

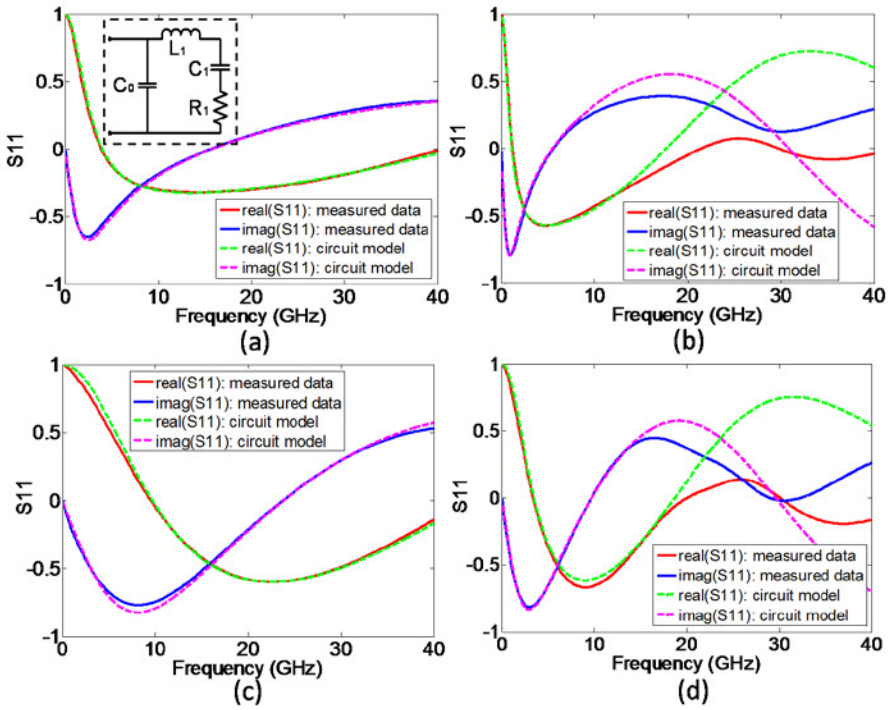


Fig. 8. S11 measurement together with curve fitting result. The reverse bias is 0 V. (a) interdigitated PN junction of 0.5 mm. (b) interdigitated PN junction of 1.5 mm. (c) lateral PN junction of 0.5 mm. (d) lateral PN junction of 1.5 mm.

**Table 1. RLC model of lumped electrode (doping concentration of $1 \times 10^{18}$/cm$^3$)**

| Doping pattern | lateral PN junction 0.5 mm | lateral PN junction 1.5 mm | interdigitated PN junction 0.5 mm | interdigitated PN junction 1.5 mm |
|---|---|---|---|---|
| $C_0$ (fF) | 26 | 83 | 24 | 80 |
| $C_1$ (pF) | 0.26 | 0.75 | 0.84 | 2.7 |
| $R_1$ (Ω) | 12.7 | 12.1 | 25.6 | 13.6 |
| $L_1$ (nH) | 0.176 | 0.374 | 0.138 | 0.327 |
| $R_1$ at DC (Ω) | 6.6 | 5.7 | 6.4 | 6.3 |
| $C_1$ at 100 kHz (pF) | 0.22 | 0.66 | 0.80 | 2.40 |

The electro-optic RF performance is then carried out by measuring the frequency response S21 of the electro-optic modulation. A bias tee is used to add a DC bias to the applied RF

#166477 - $15.00 USD Received 12 Apr 2012; revised 12 May 2012; accepted 13 May 2012; published 23 May 2012

signal. The biased RF signal is then fed into the sample by a high speed GSG probe. During the eye diagram measurement, the modulated optical signal passes through an Erbium Doped Fiber Amplifier (EDFA) and a band pass filter in sequence before finally going to a digital communication analyzer with an optical head. Figures 9 and 10 show the frequency responses (the electrical definition of the modulation response is utilized here) and eye diagrams of MZ modulators with the two doping patterns. The practical electrical 3 dB bandwidths at 0 V reverse bias are 2.6 GHz and 1.0 GHz for the interdigitated PN junctions of 0.5 mm and 1.5 mm respectively, and 10 GHz and 3.6 GHz for lateral PN junctions of the same lengths. These values agree well with the prediction of RLC model. On the other hand, the optical 3 dB bandwidths, i.e., the electrical 6 dB bandwidth, at 0 V reverse bias are 4.3 GHz and 2.1 GHz for the interdigitated PN junctions of 0.5 mm and 1.5 mm respectively, and 12.6 GHz and 5.5 GHz for the lateral PN junctions of the same lengths.

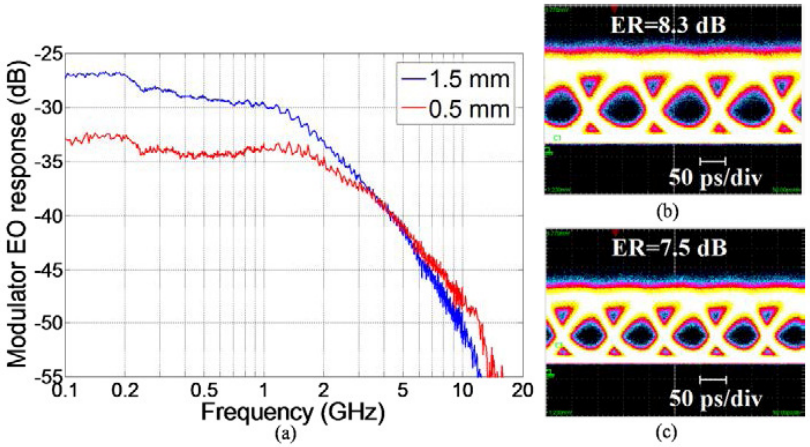


Fig. 9. EO frequency responses (the electrical definition) and eye diagrams of MZ modulators with the interdigitated PN junction. The doping concentration is $1 \times 10^{18}/cm^3$. (a) EO frequency responses for different phase shifter lengths at 0 V. (b) 8 Gbit/s eye diagram of 0.5 mm phase shifter. (c) 10 Gbit/s eye diagram of 0.5 mm phase shifter. In (b) and (c) the reverse bias is –2.5 V, and the peak-to-peak voltage of $2^{15}$–1 PRBS signal is 3 V.

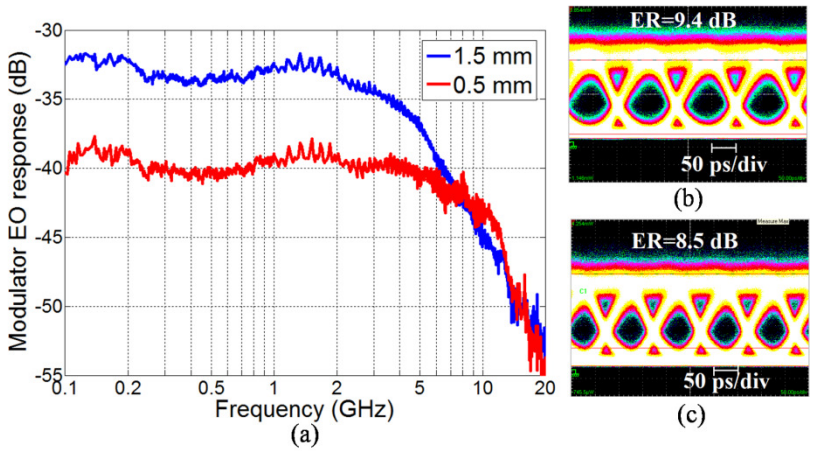


Fig. 10. EO frequency responses and eye diagrams of MZ modulators with the lateral PN junction. The doping concentration is $1 \times 10^{18}/cm^3$. (a) EO frequency responses for different phase shifter lengths at 0 V. (b) 8 Gbit/s eye diagram of 1.5 mm phase shifter. (c) 10 Gbit/s eye diagram of 1.5 mm phase shifter. In (b) and (c) the reverse bias is –1.5 V, and the peak-to-peak voltage of $2^{15}$–1 PRBS signal is 2 V.

#166477 - $15.00 USD Received 12 Apr 2012; revised 12 May 2012; accepted 13 May 2012; published 23 May 2012

Next, eye diagrams were measured using non-return-to-zero (NRZ) pseudorandom bit sequences (PRBS) at different bit rates. The results are shown for different bit rates in Figs. 9 and 10, for the 0.5 mm interdigitated and the 1.5 mm lateral PN junctions respectively. The peak-to-peak voltages $V_{pp}$ of input PRBS signals from the signal generator to the DUT and the reverse biases are 3 $V_{pp}$ and −2.5 V for the 0.5 mm interdigitated PN junction, and 2 $V_{pp}$ and −1.5 V for the 1.5 mm lateral PN junction. Due to a superposition between the input and the reflected RF signals, the practical voltage swing applied to the PN junction capacitor is estimated to be around two times as large as the signal originating from the PRBS generator.

With proper phase shifter lengths, both lateral and interdigitated PN junctions are able to operate at 10 Gbit/s when driven from a lumped electrode. Owing to its high modulation efficiency, the interdigitated PN junction based MZ can enable an ER of more than 8 dB from a much shorter device length as compared to the lateral PN junction based device (0.5 mm vs. 1.5 mm). On the other hand, the lateral and the interdigitated PN junctions have very similar propagation loss (2.3 dB/mm vs. 2.5 dB/mm) as shown in Fig. 7. As such, the total insertion loss of interdigitated junction based device is much less (2.8 dB for 0.5 mm device) than that of the lateral PN junction based device (5 dB for 1.5 mm device). However, the high capacitance accompanying the high modulation efficiency will hinder the interdigitated PN junction based device for modulation faster than 10 Gbit/s, although speed improvements can be expected for interdigitated diodes with reduced finger overlap *L*. In the next section, we discuss how the low capacitance of lateral PN junction helps to achieve 40 Gbit/s modulation.

## 5. MZs with the traveling wave electrode

In this section, we utilize the coplanar waveguide (CPW) to improve the operation speed of MZ modulator. RF design is carried out by building an equivalent circuit model of CPW with conformal mapping and partial capacitance techniques. The model then allows us to optimize the CPW for maximal modulation bandwidth [19]. Based on our RF calculation, the width of the central signal metal electrode is set to 6 μm, and the gap between the signal metal and the two ground planes is set to 3.5 μm. A microscope image of the CPW is shown in Fig. 11. Both for the lateral and intedigitated PN junctions, the phase shifter length and the doping concentration are 3 mm and $2 \times 10^{18}/cm^3$ respectively.

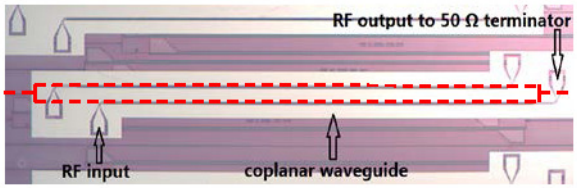


Fig. 11. Microscope images of the traveling wave electrodes to drive the 3 mm phase shifter. The dashed lines delineate the position of waveguide.

The operation speed of MZ modulators with the traveling wave electrode is characterized on the measurement platform of KIT whose bit rate ranges from 25 Gbit/s to 40 Gbit/s. The driving signal reaching the input port of CPW is around 5 $V_{pp}$. The output port of CPW is terminated with a 50 Ω load. Eye diagrams of the lateral PN junction are presented in Fig. 12. Although the pattern effect becomes an issue above 35 Gbit/s, the eye is marginally open at 40 Gbit/s. The obtained extinction ratios at 25 Gbit/s and 35 Gbit/s are 11.74 dB and 11.26 dB respectively. Error free operation (BER<$2 \times 10^{-10}$) is achieved at 35 Gbit/s as shown in Fig. 13. The 3 dB optical modulation bandwidth is measured to be 15 GHz at −4 V, which agrees well with the prediction of our equivalent circuit model [19]. The effective permittivity, attenuation coefficient and characteristic impedance of the CPW at this frequency and bias are 16, 2.6 dB/mm, and 33 Ω respectively. More details about the transmission line design and characterization can be found in [19].

#166477 - $15.00 USD Received 12 Apr 2012; revised 12 May 2012; accepted 13 May 2012; published 23 May 2012

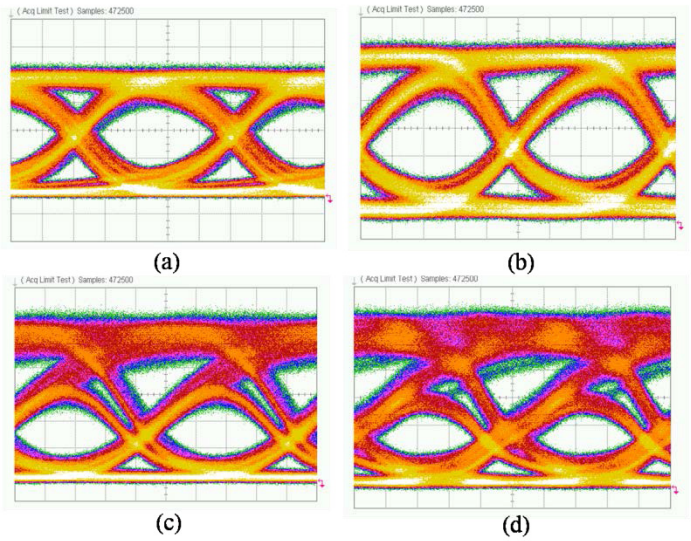


Fig. 12. Eye diagrams of the MZ modulator with the lateral PN junction and the traveling wave electrode: (a) 25 Gbit/s. (b) 28 Gbit/s. (c) 35 Gbit/s. (d) 40 Gbit/s. Pattern length of the PRBS sequence is $2^7$–1. The DC reverse biases are –5 V, –6 V, –6.2 V and –6.2 V for (a), (b), (c) and (d) respectively. The optical wavelength is fixed at 1555 nm.

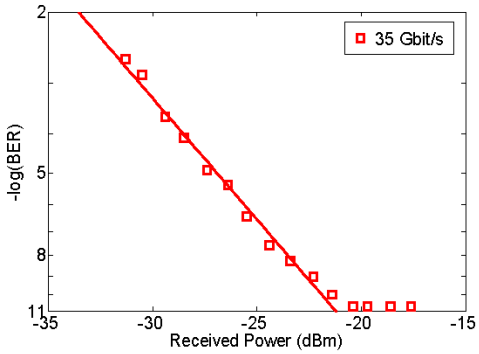


Fig. 13. Bit error rate of the MZ modulator with the lateral PN junction and the traveling wave electrode at 35 Gbit/s.

On the other hand, the interdigitated PN junction with the same traveling wave electrode doesn't provide open eye diagrams at 25 Gbit/s, which is the lowest bit rate of the measurement setup. The operation speed of any modulator with the traveling wave electrode is determined by 3 factors, i.e., the velocity matching, the impedance matching and the microwave attenuation. Our calculation shows that for the 3mm interdigitated PN junction here, its high depletion capacitance leads to a high microwave attenuation (5.4 dB/mm at 15 GHz) which is the major limitation of the operation speed. This can be understood intuitively by the fact that a large depletion capacitance results in a large shunt admittance between the signal electrode and the ground. It therefore increases the axial current running along the electrode [20]. The conductor loss is always proportional to the square of current. The high microwave loss can be mitigated by cutting the phase shifter length.

## 6. Conclusion

In this paper, lateral and interdigitated PN diode junctions are compared systematically in terms of electr-optic modulation efficiency, optical loss and depletion capacitance. After an

#166477 - $15.00 USD Received 12 Apr 2012; revised 12 May 2012; accepted 13 May 2012; published 23 May 2012

optimization to the doping patterns, a high modulation efficiency of $V_\pi L_\pi$ = 0.62 V and a high modulation speed of 40 Gbit/s are demonstrated with the interdigitated and the lateral PN junctions respectively. The performance of the two PN junctions based phase shifters and MZ modulators are summarized in Tables 2 and 3 respectively. If the lumped electrode is utilized, both lateral and interdigitated PN junctions support 10 Gbit/s modulation. At this bit rate, the MZ modulator based on the interdigitated PN junction exhibit a lower insertion loss as compared to the MZ modulator based on the lateral diode, owing to the higher modulation efficiency of the former at equal optical loss. On the other hand, the lateral PN junction is superior to the interdigitated PN junction for modulation rates beyond 10Gb/s, owing to its much lower depletion capacitance. As such, the optimum choice between the two PN junctions depends on the requirements of the application of interest.

**Table 2. Performance of interdigitated and lateral PN junctions based phase shifters**

| **Doping pattern** | **Lateral PN junction ($10^{18}$/cm$^3$)** | **Interdigitated PN junction ($10^{18}$/cm$^3$)** | **Lateral PN junction ($2 \times 10^{18}$/cm$^3$)** | **Interdigitated PN junction ($2 \times 10^{18}$/cm$^3$)** |
|---|---|---|---|---|
| $V_\pi L_\pi$ at –1 V (V·cm) | 1.55 | 1.12($W$ = 300nm) | 1.19 | 0.62($W$ = 250nm) |
| $V_\pi L_\pi$ at –6 V (V·cm) | 2.06 | 1.5 ($W$ = 300nm) | 1.23 | 0.96($W$ = 250nm) |
| Propagation loss at 0 V (dB/mm) | 2.3 | 2.5($W$ = 300nm) | 4.6 | 3.4($W$ = 250nm) |
| Depletion capacitance per unit length (pF/mm) | 0.44 | 1.59 | ~ | ~ |

**Table 3. Performance of interdigitated and lateral PN junctions based MZ modulators**

| **Doping pattern** | **Lateral PN junction ($10^{18}$/cm$^3$)** | **Interdigitated PN junction ($10^{18}$/cm$^3$)** | **Lateral PN junction ($2 \times 10^{18}$/cm$^3$)** | **Interdigitated PN junction ($2 \times 10^{18}$/cm$^3$)** |
|---|---|---|---|---|
| Lumped electrode length for 10 Gbit/s modulation (mm) | 1.5 | 0.5 | ~ | ~ |
| Optical 3 dB bandwidth with the lumped electrode (GHz) | 5.5 | 4.3 | ~ | ~ |
| Electrical 3 dB bandwidth with the lumped electrode (GHz) | 3.6 | 2.6 | ~ | ~ |
| ER at 10 Gbit/s with the lumped electrode (dB) | 8.5 | 7.5 | ~ | ~ |
| $V_{pp}$ with the lumped electrode (V) | 2 | 3 | ~ | ~ |
| Insertion loss with the lumped electrode (dB) | 5 | 2.8 | | |
| Bit rate with 3 mm CPW | ~ | ~ | 35 Gbit/s | ~ |
| ER with 3 mm CPW | ~ | ~ | 11.3dB@35Gbit/s | ~ |


## Acknowledgments

This work was supported by imec's Core Partner Program. High-speed characterization was done in the framework of the European FP7 project SOFI (grant 248609). The authors Dietmar Korn and David Hillerkuss acknowledge financial support from the Karlsruhe School of Optics & Photonics (KSOP) and the German Research Foundation (DFG).


#166477 - $15.00 USD Received 12 Apr 2012; revised 12 May 2012; accepted 13 May 2012; published 23 May 2012